Supporting Information

Induction heating: an efficient methodology for the synthesis of functional core-shell nanoparticles

Álvaro Raya-Barón,[#,a] Sourav Ghosh,[#,a] Jaime Mazarío,[#,a] Víctor Varela-Izquierdo,[a] Pier-Francesco Fazzini,[a] Simon Tricard,[a] Jerome Esvan,[b] Bruno Chaudret[a,*]

[a]*LPCNO (Laboratoire de Physique et Chimie des Nano-Objets), Université de Toulouse, CNRS, INSA, UPS, 31077 Toulouse, France.*

[b]*CIRIMAT-ENSIACET, INP-ENSIACET, 4 allée Emile Monso, BP 44362, 31030 Toulouse cedex 4, France.*

[#]Equally contributed

[*]Corresponding author Email address: chaudret@insa-toulouse.fr

Table of Contents

1. Experimental Methods

1.1. General methods

All air-sensitive procedures were carried out either under an inert atmosphere of argon inside a glovebox or in a double vacuum/Ar line. The solvents employed for nanoparticle synthesis were purchased from VWR, dried by passage through alumina in a Solvent Purification System and then further degassed by bubbling argon for 20 minutes prior to use. Palmitic acid (PA), hexadecyl amine (HDA), $Mo(CO)_6$, and $W(CO)_6$ were purchased from Sigma Aldrich and used without further purification. Metal precursors $Fe[((CH_3)_3Si)_2N]_2$ and $Ni[^iPrNC(CH_3)N^iPr]_2$ were obtained from Nanomeps. Siralox (Siralox 5/320, 5% SiO_2 doped Al_2O_3) was obtained from Sasol.

1.2. Synthesis of FeNi$_3$ NPs

The synthesis of FeNi$_3$ NPs has been previously described by our group.[1] Briefly, in a glovebox, a solution of PA (185 mg, 0.72 mmol) in 8 mL of mesitylene was added upon a mixture of $Fe[N(Si(CH_3)_3)_2]_2$ (301 mg, 0.4 mmol) and $Ni[^iPrNC(CH_3)N^iPr]_2$ (682 mg, 2 mmol) dissolved in 12 mL of mesitylene inside a Fisher-Porter (FP) bottle. The vessel was pressurized with H_2 (3 bar), placed in a pre-heated oil bath at 150°C and stirred for 24 h. Then, the magnetic product was decanted with a magnet and washed with toluene (3x5 mL), then dried under reduced pressure. This procedure yields 130-150 mg of FeNi$_3$ NPs with a metal content of 85-90 w%, determined by TGA, and a composition of ca. 28 w% Fe and 69 w% Ni, determined by ICP-AES.

1.3. Synthesis of Fe$_{2.2}$C NPs

The synthesis of Fe$_{2.2}$C NPs has been previously described by our group.[2] Briefly, a solution containing 753.2 mg (1 mmol) of $Fe[N(Si(CH_3)_3)_2]_2$, 666.4 mg (2.62 mmol) of PA and 483.0 mg (2 mmol) of HAD in mesitylene (40 mL) was pressurized with H_2 (2 bar) and stirred within an oil bath at 150ºC for 3 days. Next, the magnetic product was decanted, washed with toluene (3x10 mL) and THF (3x10 mL), and dried, affording ~100 mg of Fe(0) NPs that were employed in the next step of synthesis as obtained. The Fe(0) NPs (100 mg) were dispersed in a solution of PA (56 mg) and Et_3N (3 drops) in mesitylene (20 mL), and the mixture was pressurized with CO (2 bar) and H_2 (2 bar) and stirred within an oil bath at 150ºC for 6 days. Then, the magnetic product was decanted, washed with toluene (3x10 mL) and dried under vacuum, affording 85-100 mg of Fe$_{2.2}$C NPs with a metal content of ~75 wt% determined by TGA.

1.4. Synthesis of FeNi₃@Mo-TH and Fe₂.₂C@Mo-TH NPs via thermal heating

The same procedure was followed for FeNi$_3$@Mo-TH and Fe$_{2.2}$C@Mo-TH, using either FeNi$_3$ (for FeNi$_3$@Mo-TH) or Fe$_{2.2}$C (for Fe$_{2.2}$C@Mo-TH) NPs as starting materials. Inside a glovebox, a Fisher-Porter bottle was charged with a dispersion of either FeNi$_3$ (70 mg, ca 1.1 mmol of metal) or Fe$_{2.2}$C (70 mg, ca 1.0 mmol of metal) in mesitylene (10 mL) and Mo(CO)$_6$ (25 mg, ca 0.01 mmol) was added as a powder to de solution. The Fisher-Porter bottle was sealed under argon atmosphere and the mixture was stirred at room temperature for 30 minutes, and then pressurized with H$_2$ (3 bar) and introduced in a pre-heated oil bath at 150 ºC. After 72 hours, the reaction was allowed to cool down to room temperature and, in the glovebox, palmitic acid (60 mg, ca 0.23 mmol) and Mo(CO)$_6$ (98 mg, ca 0.37 mmol) were added to the reaction mixture and dissolved. The vessel was sealed under Ar and the dispersion was sonicated for 20 minutes, then pressurized with H$_2$ (3 bar) and stirred in an oil bath at 150ºC for 72 hours. Then, the resulting dark suspension was allowed to cool down to room temperature while decanting with the assistance of a magnet. Inside the glovebox, the supernatant was discarded and the remaining black powder was washed with toluene (3x10 mL) and dried under reduced pressure. Yield of FeNi$_3$@Mo-TH: 64 mg. Yield Fe$_{2.2}$C@Mo-TH: 76 mg.

1.5. Synthesis of FeNi₃@Mo-IH and Fe₂.₂C@Mo-IH NPs using induction heating

Both FeNi$_3$@Mo-IH and Fe$_{2.2}$C@Mo-IH nanoparticles were prepared following the same procedure, changing only the magnetic nanoparticles used as starting material. Inside a glovebox, a Fisher-Porter bottle was charged with either FeNi$_3$ (70 mg, ca 1.1 mmol of metal) or Fe$_{2.2}$C (70 mg, ca 1.0 mmol of metal), Mo(CO)$_6$ (58 mg, 0.22 mmol) and palmitic acid (70 mg, 0.28 mmol). Mesitylene (10 mL) was added and the vessel was sealed under Ar atmosphere. The mixture was then stirred (the magnetic NPs acting as a stirring agent) for 30 min, until complete dissolution of Mo(CO)$_6$ and palmitic acid, and then pressurized with H$_2$ (3 bar). The reaction vessel was placed in a magnetic coil (300 kHz, 15 mT) during 48 h. During the course of the reaction with induction heating, reflux was observed, as well as a pressure increase of 0.5 bar and a temperature of 165 ºC (measured by an IR camera). After this time, the resulting dark suspension was allowed to cool down to room temperature while decanting with the assistance of a magnet. Inside the glovebox, the supernatant was discarded and the remaining black powder was washed with toluene (3x10 mL) and dried under reduced pressure. Yield of FeNi$_3$@Mo-IH: 90 mg. Yield of Fe$_{2.2}$C@Mo-IH: 88.5 mg.

1.6. Impregnation on Siralox

In the glovebox, the nanoparticles (either 75 mg of $FeNi_3$@Mo-IH, or 56 mg $Fe_{2.2}C$@Mo-IH, $Fe_{2.2}C$, or $FeNi_3$) and Siralox (150 mg) were suspended in THF (5 mL) inside a Fisher-Porter bottle. The mixture was sonicated for 1 hour, and then the solvent was removed under reduced pressure. The remaining black powder was further dried in vacuum at R.T. overnight and then stored under an argon atmosphere.

1.7. Synthesis of $FeNi_3$@WOx-IH

At first, $FeNi_3$@W-IH nanoparticles were prepared following a first procedure analogous to the one described for Mo-IH materials. The experiment was carried out by adding $FeNi_3$ nanoparticles (70 mg, ca 1.1 mmol of metal), $W(CO)_6$ (78 mg, 0.22 mmol), and palmitic acid (70 mg, 0.28 mmol) into a Fisher-Porter bottle within a glovebox. Then 10 mL of mesitylene was added, stirring the mixture for 30 minutes using the magnetic nanoparticles as a stirring agent until $W(CO)_6$ and palmitic acid were completely dissolved. Next, the vessel was pressurized with H_2 (3 bar) and placed in a magnetic coil (300 kHz, 15 mT) for 48 hours. Throughout the reaction, reflux occurred with a peak pressure of 3.9 bar and temperature ranging from 156 to 160 ºC, measured using an IR camera. The resulting dark suspension was left to cool down to room temperature. Then, with the help of a magnet, it was decanted. Within the glove box, the liquid portion was discarded, and the remaining black powder was washed twice with toluene (each time with 10 mL) and dried under reduced pressure. Following, an oxidation step was carried out by suspending the NPs in 10 mL toluene and opening the valve of the FP head to allow for slow air diffusion. After 24 hours, the nanoparticles were decanted with the help of a magnet and vacuum-dried. The resulting nanoparticles were named $FeNi_3$@WO_x-IH.

1.8. Morphological and Chemical Characterization

The size and the morphology of the NPs were studied by transmission electronic microscopy (TEM). TEM grids were prepared by deposition of one drop of a colloidal solution containing the NPs on a copper grid covered with amorphous carbon. Bright-field TEM (BF TEM) imaging was performed using a JEOL microscope (Model 1400) working at 120 kV. Scanning transmission electron microscopy (STEM) analyses were performed using a Probe Corrected JEOL JEM-ARM200F microscope (cold FEG source) working at 200 kV. The STEM-EDX analysis was carried out with a High Angle EDX detector attached to the TEM microscope. Thermogravimetric analyses (TGA) were performed in a TGA/DSC 1 STAR System equipped with an ultra-microbalance UMX5,

a gas switch GC200 and sensors DTA and DSC. XRD measurements were performed on a PANalytical Empyrean diffractometer using Co-Kα radiation (λ=0.1789 nm) at 35 kV and 45 mA. The powder samples are prepared and sealed under an argon atmosphere. The powder samples are prepared and sealed under an argon atmosphere. X-ray photoelectron spectra (XPS) were collected on a ThermoScientific Kalpha device at CIRIMAT Laboratory (Toulouse). Photoelectron emission spectra were recorded with Al-Kα radiation, and the sample was deposited on Al sampler holders. The spot size was 400 µm. The Pass energy was fixed at 30 eV with a step of 0.1 eV for core levels and 160 eV for surveys with a step of 1 eV. Energy calibration was done with respect to the maxima at the C*1s* region, fixed at 284.5 eV. Metal surface quantification was carried out using Ni*2p*, Fe*3p* and Mo*3d* regions for Mo-based samples, applying appropriate response sensitivity factors and correcting the intensities by using the spectrometer transmission function. Peak fitting of certain XPS regions was made using the CASAXPS software (v. 2.1.0.1), applying nonlinear-Shirley background subtractions and Gaussian-Lorentzian line shapes (see 2.5 and 2.10 sections of this SI). ATR-FTIR spectra were recorded using a Thermo Scientific Nicolet 6700 spectrophotometer using Ge tip in the range of 4000-600 cm^{-1}.

1.9. VSM measurement

Magnetic measurements were carried using a Vibrating Sample Magnetometer (VSM, Quantum Device PPMS Evercool II) by placing about 10 mg of dry powder sample in a sealed Teflon capsule inside the glovebox. The magnetization versus magnetic field measurements (hysteresis loop) were conducted at both 300 and 5 K, with an external field of up to ±3 T.

1.10. SAR measurement

The specific absorption rate (SAR) values were measured by calorimetry experiments following the protocol already described in our previous work,[1,2] using a coil with a fixed frequency of 93 kHz. In a typical experiment under inert atmosphere, a sample tube was charged with the sample Mag-NPs (around 10 mg) and dry mesitylene (0.5 mL) was added. The tube was sealed with a Teflon lined screw cap and then the mixture was sonicated during a few seconds to disperse the Mag-NPs in the solvent. During the calorimetric experiments, the sample tube was placed inside a socket filled with 1.8 mL of deionized water, in the center of the magnetic coil. Two temperature probes are submerged in the water, one near the bottom of the socket and the other near the center.

Then, the temperature increase after applying an AMF during 50 seconds is measured using different field amplitudes, which allows us to construct a curve of SAR ($W.g^{-1}$) against field amplitude (mT).

1.11. Gas phase propane dry reforming test

The gas phase propane dry reforming (PDR) test was carried out in a fixed-bed quartz reactor (internal diameter of 1 cm) in continuous flow mode. The reactor was placed at the middle of a coil capable of generating AMF with a frequency of 300 kHz. A carburization step was performed for NPs+Siralox before the PDR reaction. In a typical experiment, a mixture of 100 mg of Fe wool and 150 mg of MagNP@M-IH/Siralox (MagNP = $FeNi_3$ or $Fe_{2.2}C$; M = Mo or WO_x) is placed in a quartz reactor inside a glove box. Subsequently, the quartz reactor was placed in a 300 kHz coil. The carburization was carried out with a mixture of propane and hydrogen (C_3H_8 – 10 $mL.min^{-1}$ and H_2 – 40 $mL.min^{-1}$). The reactor temperature was maintained at ~670-680 °C by adjusting the applied magnetic field for 90 min. After the carburization, the reactor was cooled down at room temperature and the reaction gas mixture (total flow – 40 mL.min-1; C_3H_8:CO_2 molar ratio is 1:3; C_3H_8 – 10 $mL.min^{-1}$ and H_2 – 30 $mL.min^{-1}$) was introduced to the reactor. Subsequently, the reactor was heated via applying AMF at 300 kHz. Before the reaction and during the reaction, the outlet gas mixture was analyzed using GC technique. The products were identified using a PerkinElmer 580 gas chromatograph coupled with a PerkinElmer Clarus SQ8T mass spectrometer and equipped with a TCD detector. The GC method was calibrated using the know concentration of gases. The propane conversion, CO_2 conversion, and the CO selectivity were calculated using the following equations[3]:

$$X_A(\%) = \frac{C_{A_0} - C_A}{C_{A_0} + \varepsilon_A C_A} \times 100 \ (\%) \quad Eqn. 1$$

$$\varepsilon_A = \frac{\eta_{X_{A=1}} - \eta_{X_{A=0}}}{\eta_{X_{A=0}}} \quad Eqn. 2$$

$$S_i = \frac{C_i}{\sum C_i} \quad Eqn. 3$$

where, X_A is the conversion of CO_2 and C_3H_8, and the C_{A0} and C_A are the inlet and outlet concentrations of the CO_2 and C_3H_8, respectively. The $\eta_{X_{A=0}}$ and $\eta_{X_{A=1}}$ stands for total number of moles of reactants (at zero conversion) and total number of moles of products (at complete conversion). For a feed composition of 25% C_3H_8 and 75% CO_2, the ε_A is

calculated to be 1.5. The CO selectivity was calculated based on the different carbon containing products (C_i stands for the concentration of the product i) detected in GC.

2. Supplementary Results

2.1. Elemental analysis

Table S1. Bulk chemical composition of MagNP@Mo as determined by ICP-AES analysis.

Material	Fe (at.%)[a]	Ni (at.%)[a]	Mo (at.%)[a]
FeNi$_3$@Mo-TH	21	74	5
FeNi$_3$@Mo-IH	23	67	10
Fe$_{2.2}$C@Mo-TH	92	-	8
Fe$_{2.2}$C@Mo-IH	84	-	16

[a]Atomic percentage referred to the total amount of metals.

2.2. TEM and XRD characterization of MagNP@Mo-TH NPs
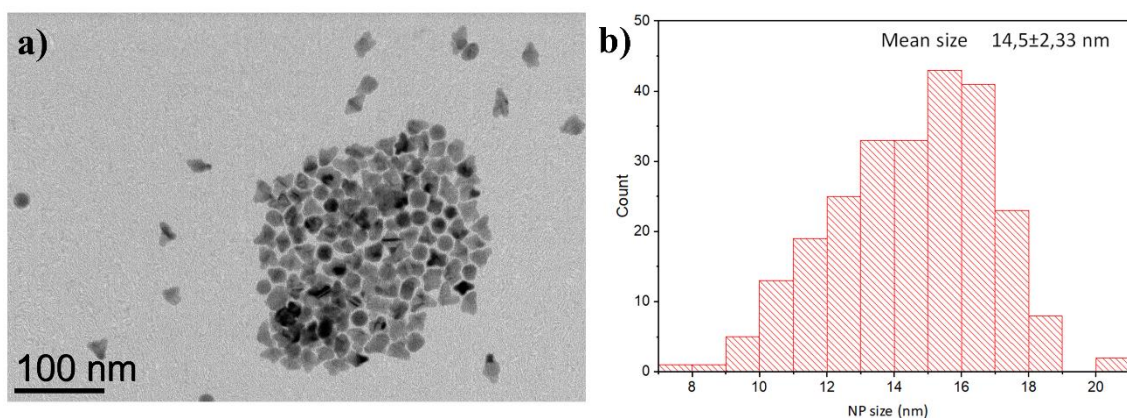
Figure S1. FeNi$_3$ NPs, a) BFTEM image, and b) particle size distribution.
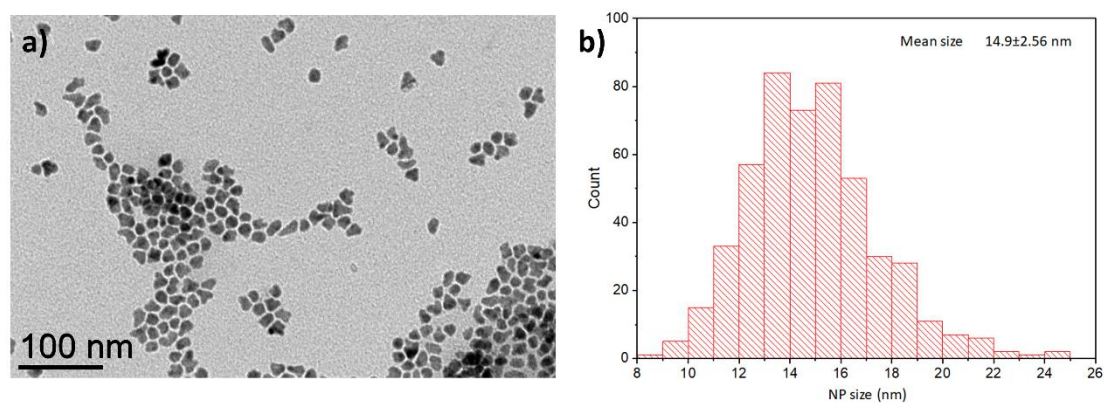
Figure S2. FeNi$_3$@Mo-TH NPs, a) BFTEM image, and b) particle size distribution.
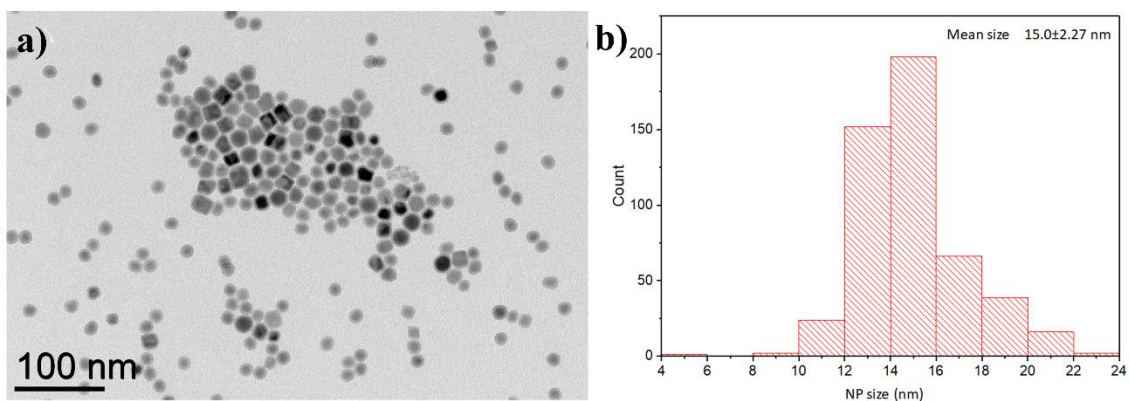
Figure S3. Fe$_{2.2}$C NPs, a) BFTEM image, and b) particle size distribution.
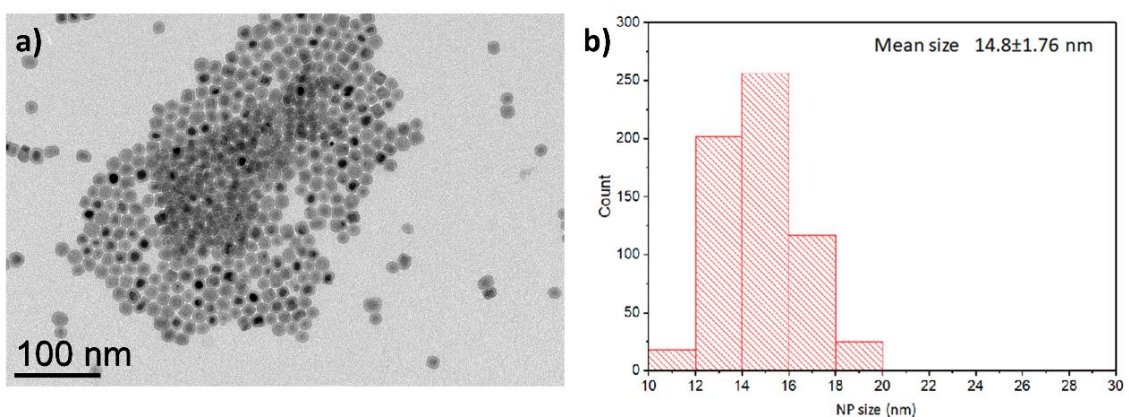
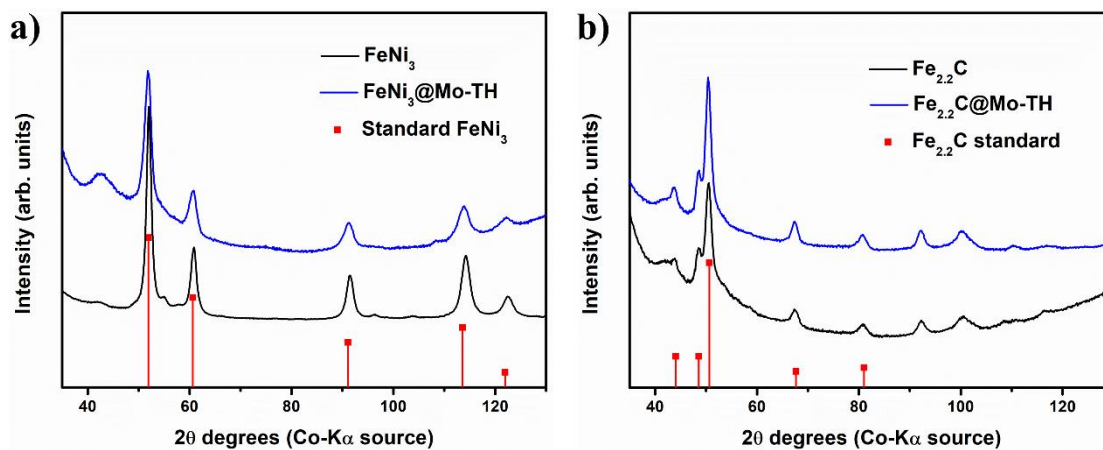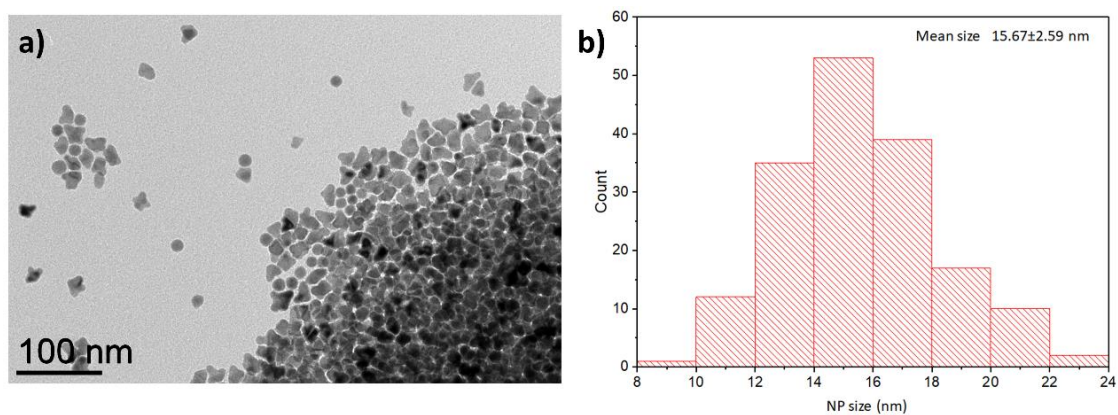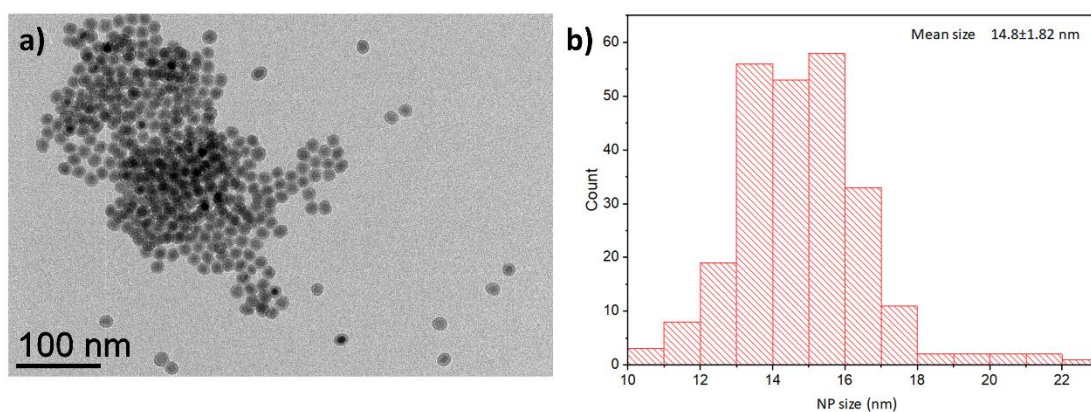**Figure S4**. Fe$_{2.2}$C@Mo-TH NPs, a) BFTEM image, and b) particle size distribution.

Figure S5. Overlay of the powder XRD patterns, a) FeNi$_3$ and FeNi$_3$@Mo-TH NPs (ICDD: 00-038-0419, standard pattern of FeNi$_3$ shown as red vertical drop lines), and b) Fe$_{2.2}$C and Fe$_{2.2}$C@Mo-TH NPs (ICDD: 00-036-1249, standard pattern of Fe$_{2.2}$C shown as red vertical drop lines).

2.3. TEM characterization of MagNP@Mo-IH NPs:

Figure S6. FeNi$_3$@Mo-IH NPs, a) BFTEM image, and b) particle size distribution.

Figure S7. Fe$_{2.2}$C@Mo-IH NPs, a) BFTEM image, and b) particle size distribution.
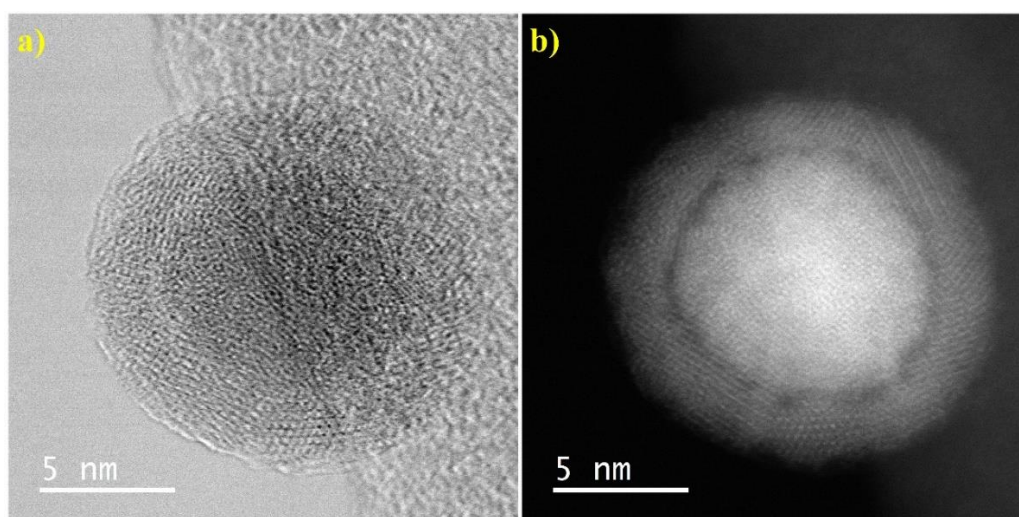

Figure S8. Fe$_{2.2}$C@Mo-IH NPs, a) HR-STEM image, and b) HR-STEM HAADF image. The contrast appears in HAADF image is due to the presence of the Mo layer and the surface FeO$_x$ of the Fe$_{2.2}$C core.
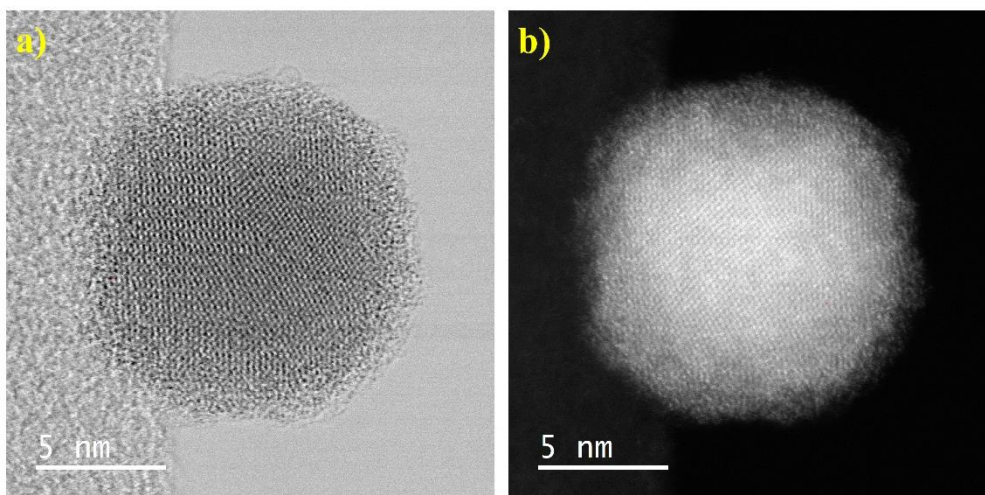
Figure S9. FeNi₃@Mo-IH NPs, a) HR-STEM image, and b) HR-STEM HAADF image.

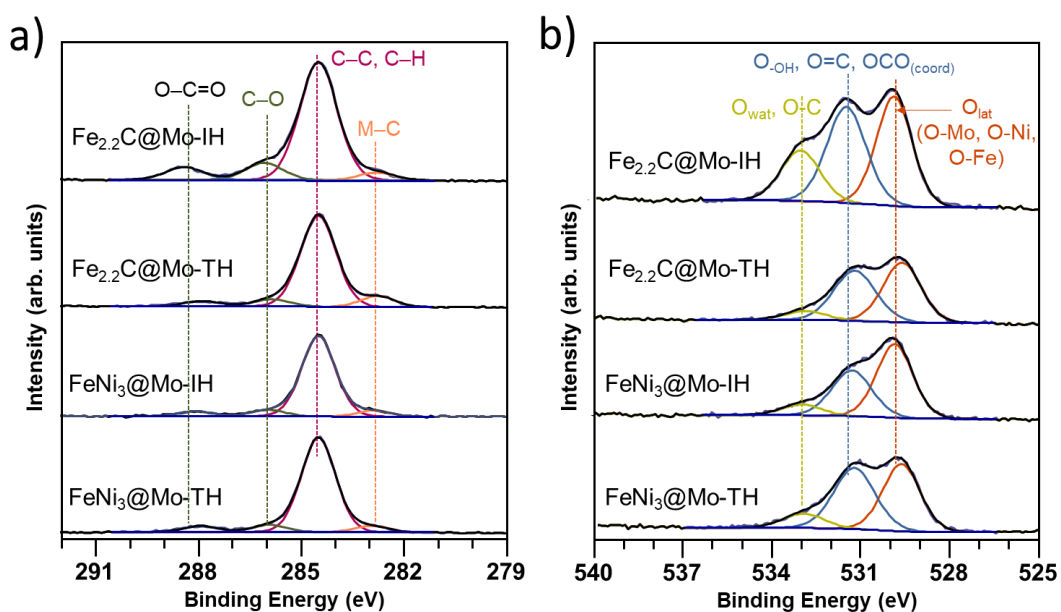## 2.4. Elemental core level XPS analyses for the Mag-NPs@Mo samples

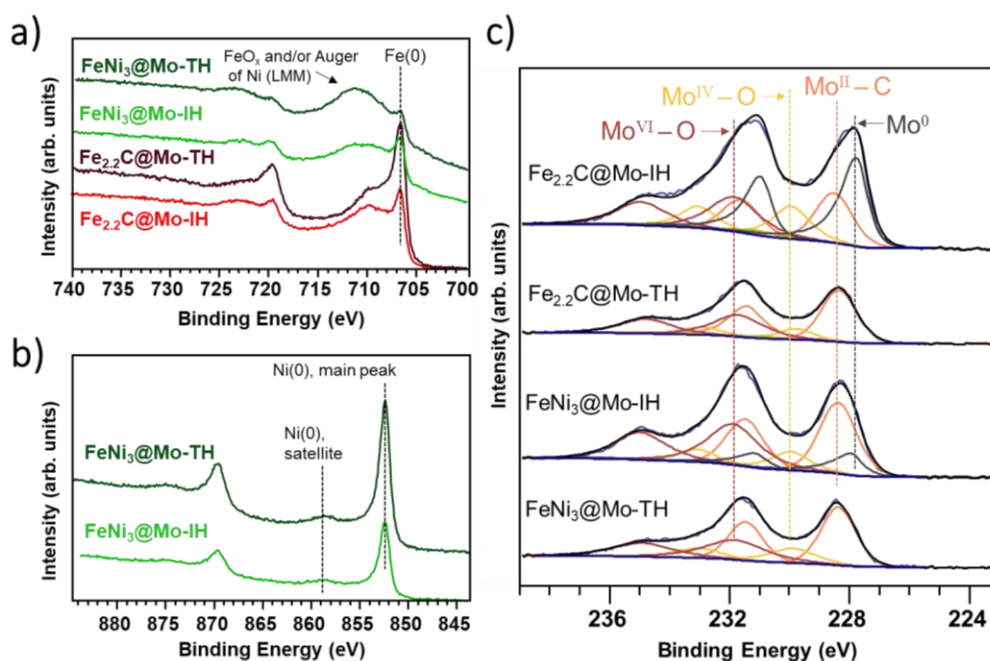**Figure S10.** a) C*1s* and b) O*1s* XPS regions for as-prepared Mo-based core-shell nanoparticles after peak fitting.

Figure S11. a) Fe2p, b) Ni2p, and c) Mo3d XPS regions for as-prepared Mo-based core-shell nanoparticles.

2.5. Fitting of the XPS Mo*3d* region in the Mag-NPs@Mo samples

During the XPS fitting of the Mo*3d* region of the as-prepared nanoparticles, B.E. restrictions and FWHM restrictions relative to Mo(IV) were applied to the *3d$_{5/2}$* oxide components (Mo^{IV}, Mo^V, Mo^{VI}). These constraints were determined using the results attained by J. Baltrusaitis *et al*. for an amorphous electrodeposited molybdenum oxide film by applying their vector analysis procedure to a subset of spectra.[4] A lower B.E. component at around 228.4 eV was also evident in all the samples, this being attributed to the carbide phase (see Main Text). Moreover, an even lower B.E. component (227.8 eV) was necessary to reasonably fit the Fe$_{2.2}$C@Mo-IH and FeNi$_3$@Mo-IH samples. This B.E. can be associated with Mo^0 and therefore given an asymmetric line shape [LA(1.1, 2.3, 2)] with an asymmetric factor of 0.3515,[5,6] as typically reported in the literature. By incorporating a metallic band, limiting the FWHM of Mo(IV) to a range between double and 1.6 times the value seen for Mo^0 becomes possible.[5,7] Regarding the line shapes for those components corresponding to Mo associated with oxygen, Gaussian-Lorentzian curves for oxidized Mo components were selected after optimizing standard residual values in this entire set of samples. A summary of all these restrictions can be found in Table S2.

Table S2. Restrictions applied in the Mo$3d$ XPS peak fitting.

Component	Parameter	Restriction
Mo(0)	Line shape	LA(1.1,2.3,2)
Mo(II) – carbidic	Line shape	GL(40)
Mo(IV), Mo(V), Mo (VI)	Line shape	GL(77)
Mo(IV)	FWHM	Mo(IV)3d$_{5/2}$: [Mo(0)3d$_{5/2}$*2, Mo(0)3d$_{5/2}$*1.6]
Mo(V)	FWHM	Mo(V)3d$_{5/2}$: Mo(IV)3d$_{5/2}$*1.2
Mo(VI)	FWHM	Mo(V)3d$_{5/2}$: Mo(IV)3d$_{5/2}$*1.4
Mo(IV)	Position	Mo(IV)3d$_{5/2}$: [229.8, 232.0]
Mo(V)	Position	Mo(V)3d$_{5/2}$: Mo(IV)3d$_{5/2}$ + 1.1
Mo(VI)	Position	Mo(VI)3d$_{5/2}$: Mo(IV)3d$_{5/2}$ + 1.9

<u>Others</u>: Mo$3d$ doublet constrains: i) same FWHM, ii) Area 3d$_{5/2}$ * 0.667= Area 3d$_{3/2}$, iii) ΔBE =[3.1, 3.2] eV.

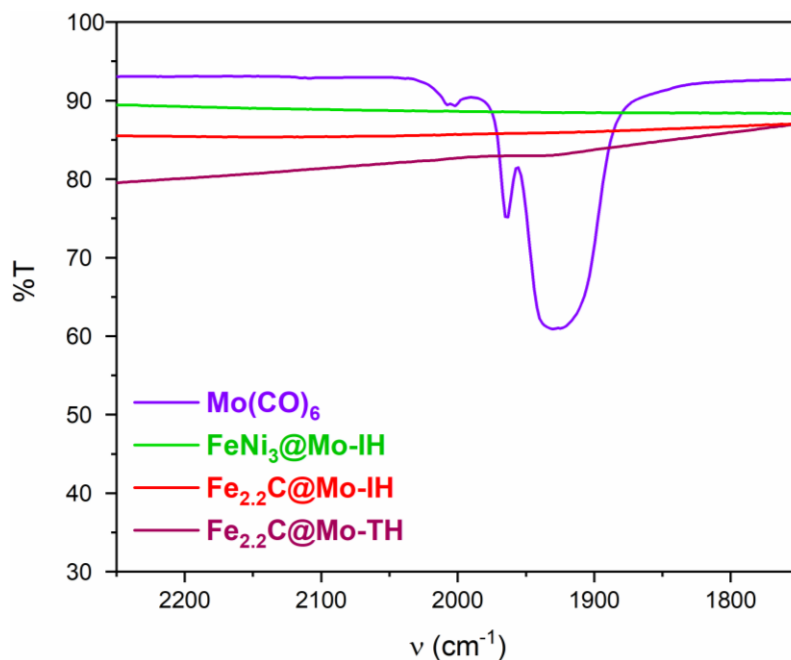## 2.6. ATR-FTIR analyses for the Mag-NPs@Mo samples

Figure S12. Selected region of the ATR-FTIR spectra for Mo(CO)$_6$ (purple), FeNi$_3$@Mo-IH NPs (green), Fe$_{2.2}$C@Mo-IH NPs (red) and Fe$_{2.2}$C@Mo-TH (garnet).

2.7. Effect of reaction temperature

Table S3. Reaction temperature of different synthesis procedure at solution phase

Materials	Thermal heating (°C)[a]	Induction heating (°C)[b]	Mo (wt.%)[c]
FeNi$_3$@Mo-TH	150	-	7
FeNi$_3$@Mo-IH	-	165	14
Fe$_{2.2}$C@Mo-TH	150	-	11
Fe$_{2.2}$C@Mo-IH	-	165	21

[a]In thermal heating, the temperature value corresponds to the temperature of the oil bath; [b]in induction heating, the temperature of the outer surface of the FP bottle was measured using an IR camera; [c]Mo loading obtained from the ICP-AES measurements, weight with respect to the total mass of the sample.

The SAR values represent the heating efficiency of the MagNPs under radio frequency pulse. The SAR values reported in the literature for FeNi$_3$ and Fe$_{2.2}$C are 600 and 2100 W.g^{-1}, respectively, and the amount of Mo deposited in the FeNi$_3$@Mo-IH and Fe$_{2.2}$C@Mo-IH are 14 and 21 wt%, respectively (Table S3). Furthermore, it is worth noting that, using the same amount of MagNPs (70 mg), the synthesis of FeNi$_3$@Mo-TH and Fe$_{2.2}$C@Mo-TH employed a total amount of 123 mg of Mo(CO)$_6$. In contrast, the procedures for FeNi$_3$@Mo-IH and Fe$_{2.2}$C@Mo-IH, using magnetic induction, only required 58 mg of Mo(CO)$_6$, while resulting in roughly twice as much Mo incorporated on the surface of the MagNPs.

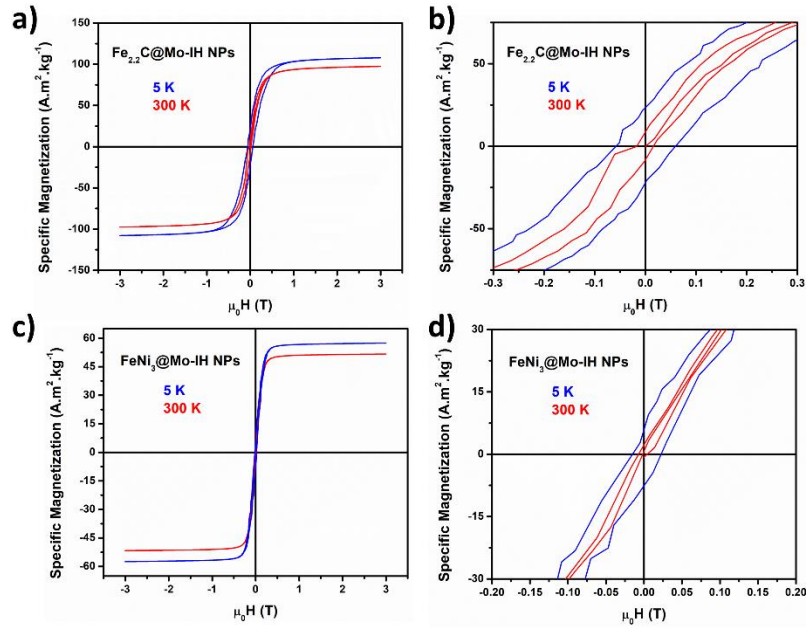## 2.8. Magnetic Properties and SAR measurements of MagNP@Mo-IH NPs

Figure S13. Magnetization versus temperature plot for $Fe_{2.2}C$@Mo-IH (a,b) and $FeNi_3$@Mo-IH (c,d), and c,d) zoomed version of figure a and b. The red and blue traces are corresponded to the measurements carried out at 300 and 5 K.

Table S4. Magnetic properties measurement of MagNP@Mo nanoparticles

Materials	T (K)	M_s (A.m^2.kg^{-1})[a]	H_c (mT)[b]
$FeNi_3$	5	94	41.4
	300	90	-
$FeNi_3$@Mo-IH	5	57	17.4
	300	52	-
$Fe_{2.2}C$	5	183	74.2
	300	162	42.3
$Fe_{2.2}C$@Mo-IH	5	108	60.5
	300	97	24.7

[a]Saturation magnetization; [b]coercive field.
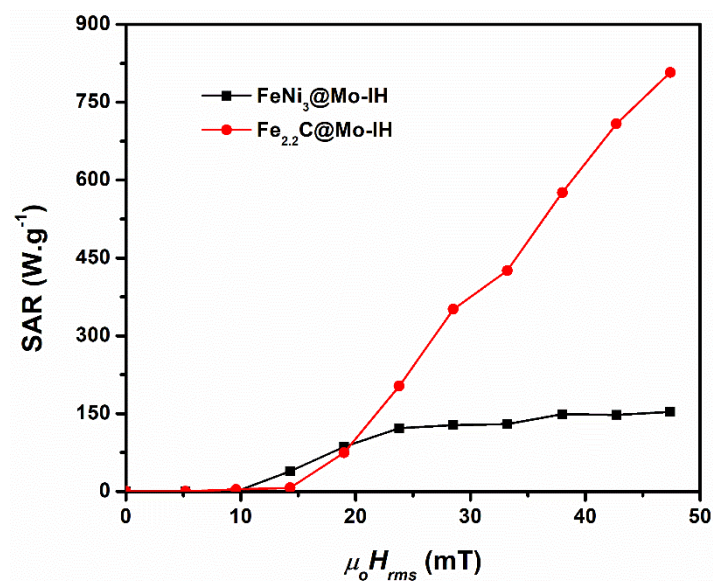
Figure S14. The heating power of FeNi$_3$@Mo-IH and Fe$_{2.2}$C@Mo-IH was evaluated through specific absorption rate (SAR) measurement. SAR measurement of FeNi$_3$@Mo-IH (black) and Fe$_{2.2}$C@Mo-IH (red) in mesitylene solution at 47 mT and 93 kHz.
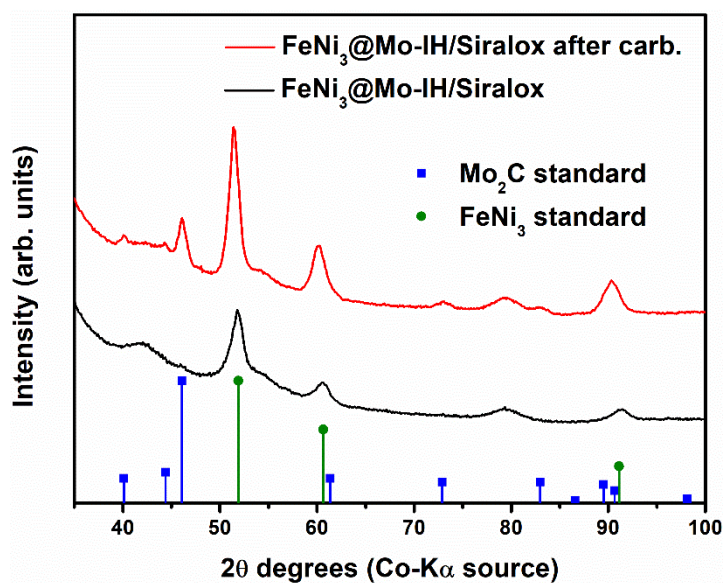
2.9. Characterization of the carburized samples

Figure S15. Overlay of the powder XRD patterns of FeNi$_3$@Mo-IH/Siralox samples before (black trace) and after (red trace) carburization (ICDD: 00-038-0419, standard pattern of FeNi$_3$ shown as green vertical drop lines; ICDD: 00-035-0787, standard pattern of Mo$_2$C shown as blue vertical drop lines).

2.10. Fitting of the XPS Mo*3d* region in carburized FeNi$_3$@Mo-IH/Siralox

Since the XRD of this sample, together with the TEM analyses unveiled a significant crystallization and growth of Mo$_2$C, the fitting of this Mo*3d* spectra is likely to present a significant level of asymmetry for the Mo$_2$C and, therefore, be hardly comparable with the latter observed for the as-prepared core-shell nanoparticles and deserves further attention. This phenomenon is expected when increasing the dimensions of the Mo carbide.[8-10]

First, the previously built model for Mo*3d* in the as-prepared nanoparticles was extended to this sample. Additional constraints were applied to FWHM and peak position for the metallic band to force it to be in good agreement with those values resulting from the former fitting. The goodness of two fitting models was tested. First, and since Mo$_2$C was detected by XRD after carburization, the area for the carbide signal in the Mo3d$_{5/2}$ region was forced to comply with that of the C*1s* signal corresponding to carbide (considering stoichiometry and R.S.F.). Second, the area was allowed to vary, which means assuming a part of the carbide may still present a different stoichiometry (amorphous, other carbide phases or oxycarbides). Figure S16 depicts how both models are insufficient in adapting to the system accurately:
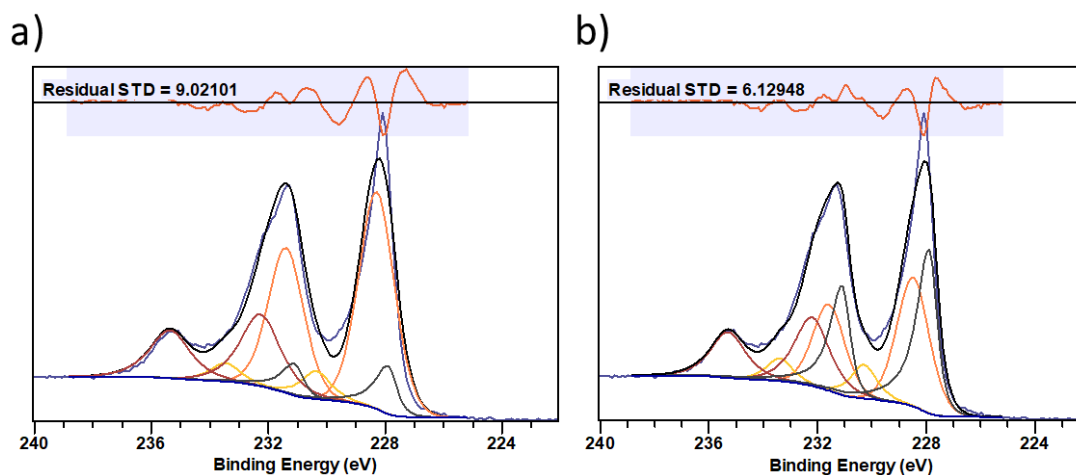

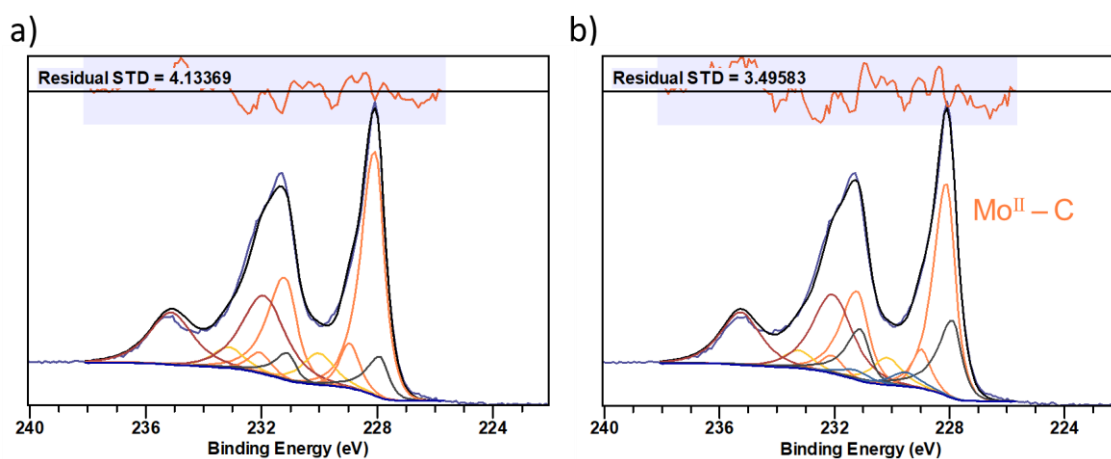**Figure S16.** Different fittings tests for the Mo*3d* region in the FeNi$_3$@Mo-IH/Siralox sample after carburization. (a) Constrain for carbidic Mo*3d$_{5/2}$* based on C*1s* carbidic area. (b) No constrain for carbidic Mo*3d$_{5/2}$*.

Finally, we opted for a combination of our model with that presented by Y. Román-Leshkov and co-workers in their recent NAP-XPS study.[11] In this report, an asymmetric line shape for Mo$_2$C, and their two satellites, forming a total of 3 doublets, was established

by DFT calculations. On the other hand, XPS fitting parameters for Mo$3d_{5/2}$ (B.E., FWHM, G/L ratios) and constraints for Mo$3d_{3/2}$ peaks in reference to their respective Mo$3d_{5/2}$ peaks were determined from multiple spectra treatment. The result of this new fitting can be found in Figure SXa and gets closer to the experimental data. Additionally, introducing an additional doublet that would correspond to an oxycarbide phase and, therefore, releasing the restriction for the area of the carbide Mo$3d_{5/2}$ signal, can further improve the fitting (Figure SXb). Notably, for the oxycarbide, a B.E. constrain [229.8, 229.2][12,13] and the same FWHM and G/L ratio than that described for the oxide were applied. These last adjustments, though they can still be improved, confirm the presence of a well-crystallized Mo$_2$C phase after the carburization process before catalysis:

Figure S17. Different fittings tests for the Mo$3d$ region in the FeNi$_3$@Mo-IH/Siralox sample after carburization. (a) After applying fittings parameters for Mo$_2$C reported by Murugappan et. al.,[11] (b) Same fitting but introducing an additional component for molybdenum oxycarbide.

Remarkably, this last model for the carbide could not fit the experimental data for the as-prepared Mag-NP@Mo samples with the same goodness as the previous model with only one symmetric Gaussian-Lorentzian doublet for the carbidic molybdenum. Together with TEM and XRD observations, this constitutes another evidence of the growth and crystallization of Mo$_2$C during the carburization step.

In the same way, trying to insert only the oxycarbide band was prevented by the model developed for the as-prepared Mag-NP@Mo samples and did not result in any further improvement in the fitting of the Mo$3d$ region in the as-prepared samples. Nevertheless, the existence of oxycarbides in these samples cannot be discarded. We believe that, given the proximity of oxycarbides to the Mo(IV) oxide binding energy, the band assigned to

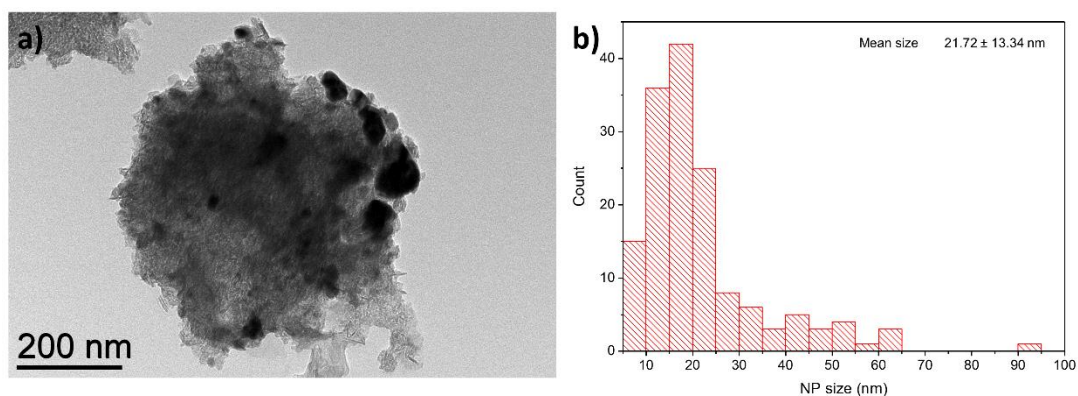Mo^{IV} in the Mag-NP@Mo samples may also include a contribution from oxycarbide phases.

Figure S18. FeNi$_3$@Mo-IH/Siralox sample after carburization, a) BFTEM image, and b) particle size distribution.
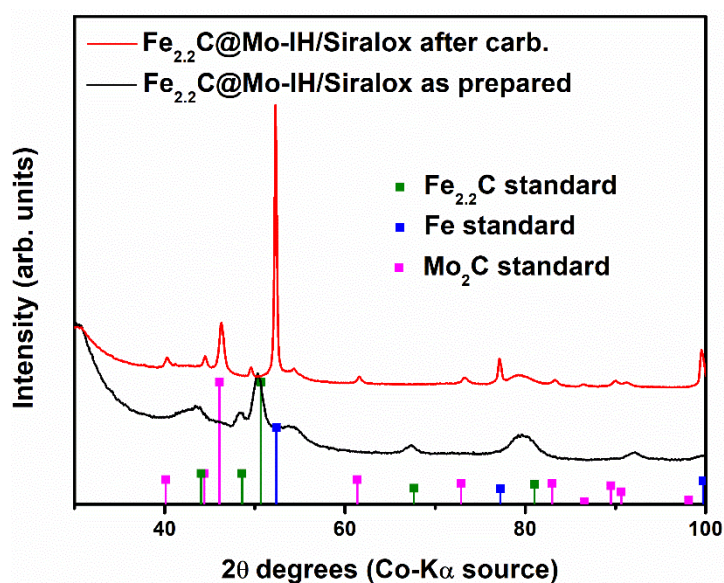

Figure S19. Overlay of the powder XRD patterns of Fe$_{2.2}$C@Mo-IH/Siralox samples before (black trace) and after (red trace) carburization (ICDD: 00-036-1249, standard pattern of Fe$_{2.2}$C shown as green vertical drop lines; ICDD: 00-035-0787, standard pattern of Mo$_2$C shown as magenta vertical drop lines; ICDD: 00-006-0696, standard pattern of Fe shown as blue vertical drop lines).
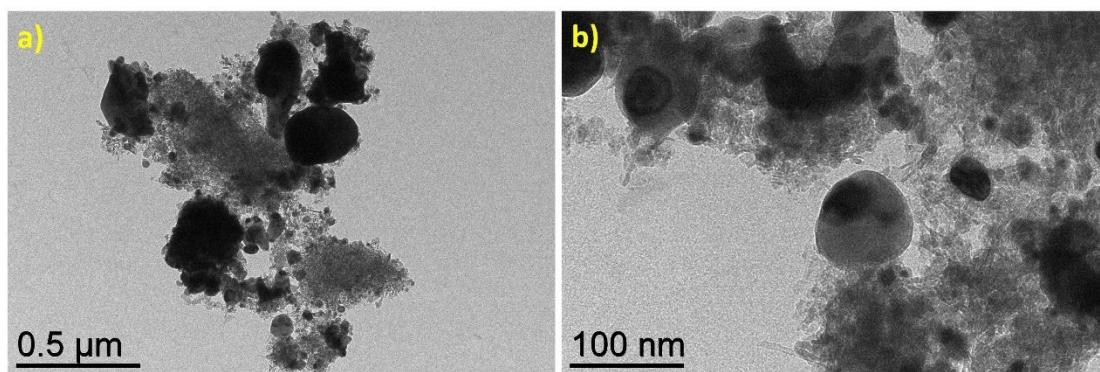
Figure S20. Fe$_{2.2}$C@Mo-IH/Siralox sample after carburization, a,b) BFTEM image.

2.11. Characterization of as-prepared and spent catalysts

Table S5. Bulk chemical composition of as-prepared MagNP@Mo-IH/Siralox as determined by ICP-AES analysis.

Material	Fe (wt.%)[a]	Ni (wt.%)[a]	Mo (wt.%)[a]
FeNi$_3$@Mo-IH/Siralox	5.4	17.7	4.5
Fe$_{2.2}$C@Mo-IH/Siralox	19.2	-	6.1

[a]Atomic percentage referred to the total amount of metals.
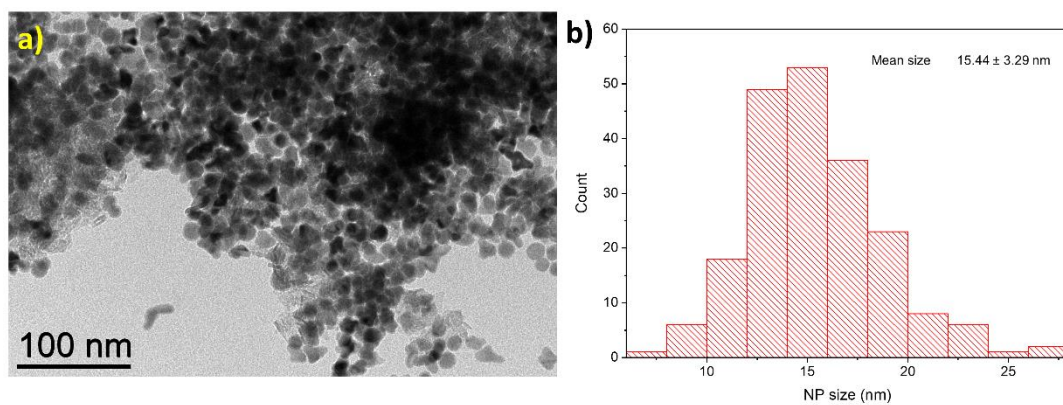
Figure S21. As prepared FeNi$_3$/Siralox, a) BFTEM image, and b) particle size distribution.
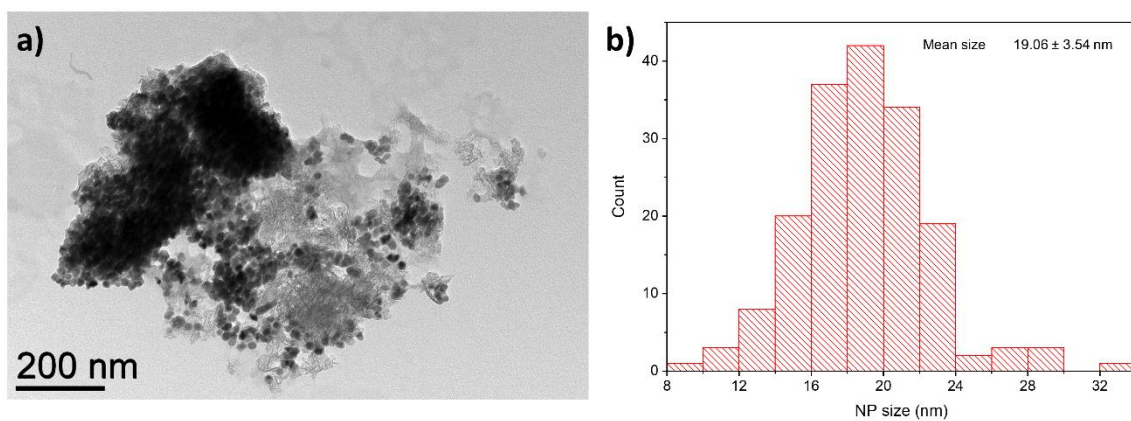
Figure S22. As prepared FeNi$_3$@Mo-IH/Siralox, a) BFTEM image, and b) particle size distribution.
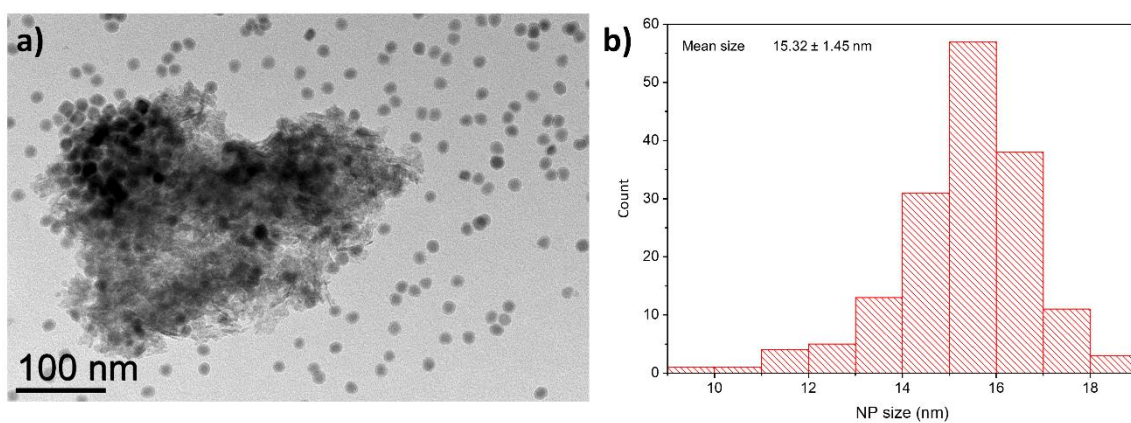
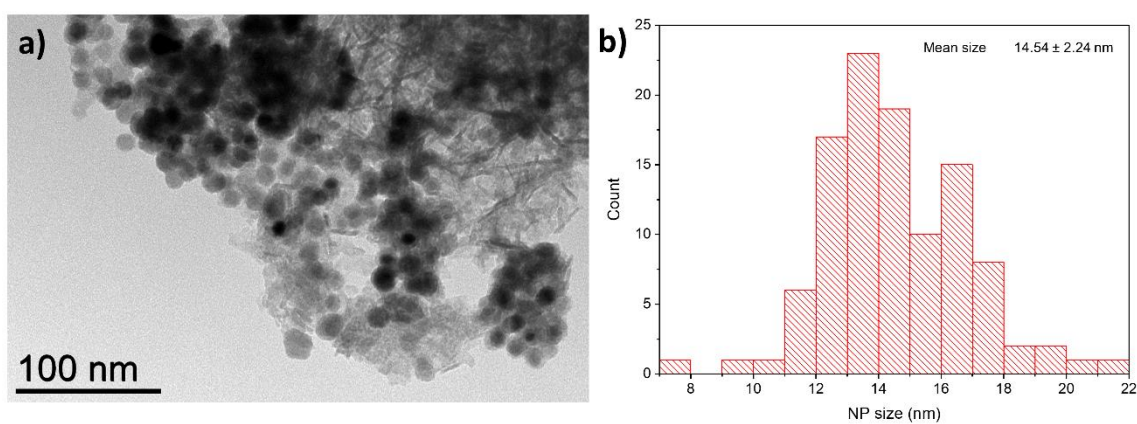**Figure S23.** As prepared Fe$_{2.2}$C/Siralox, a) BFTEM image, and b) particle size distribution.

Figure S24. As prepared Fe$_{2.2}$C@Mo-IH/Siralox, a) BFTEM image, and b) particle size distribution.

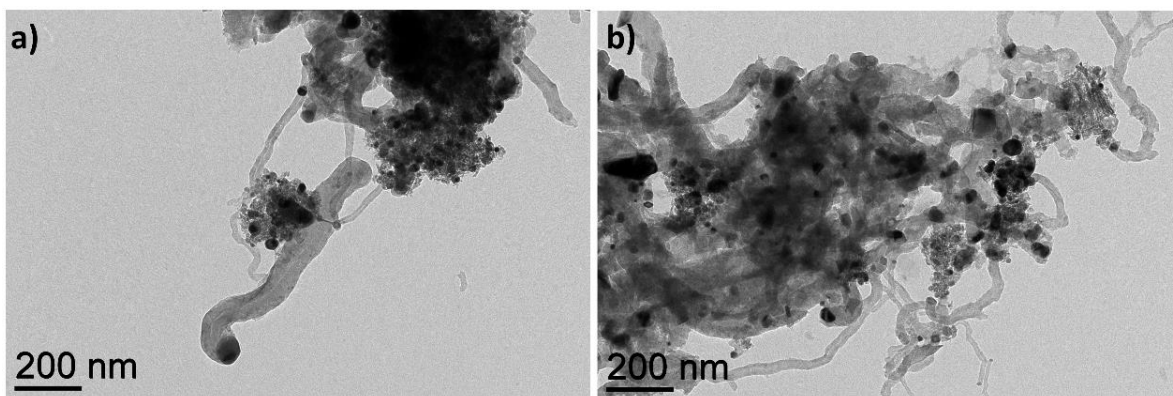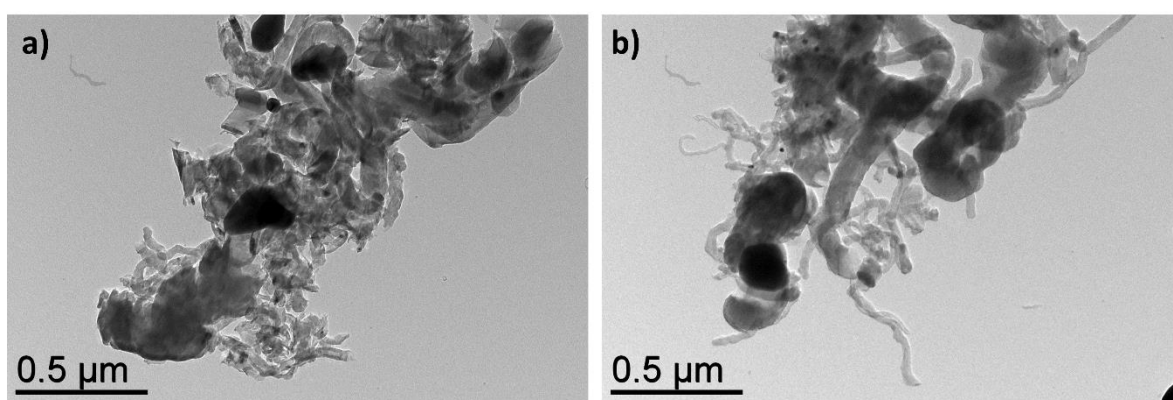**Figure S25.** Spent catalyst FeNi$_3$/Siralox, a,b) BFTEM image.

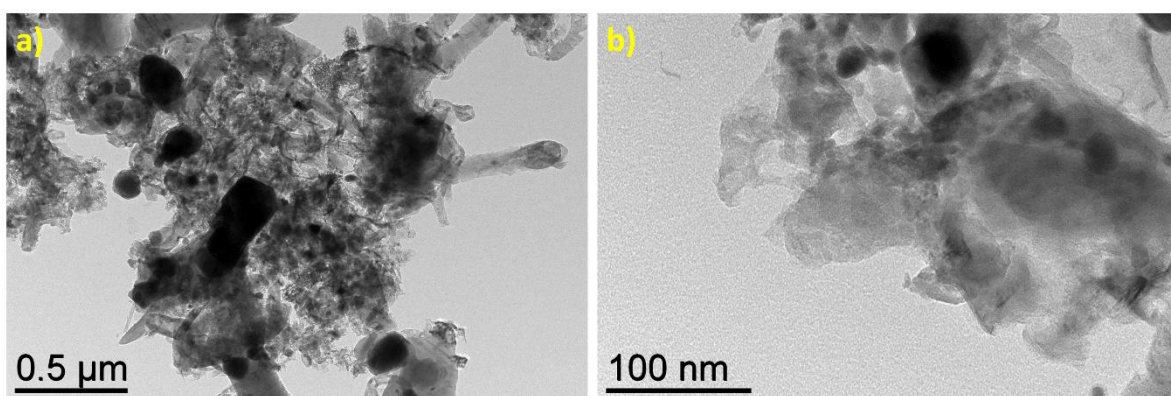**Figure S26.** Spent catalyst FeNi$_3$@Mo-IH/Siralox, a,b) BFTEM image.

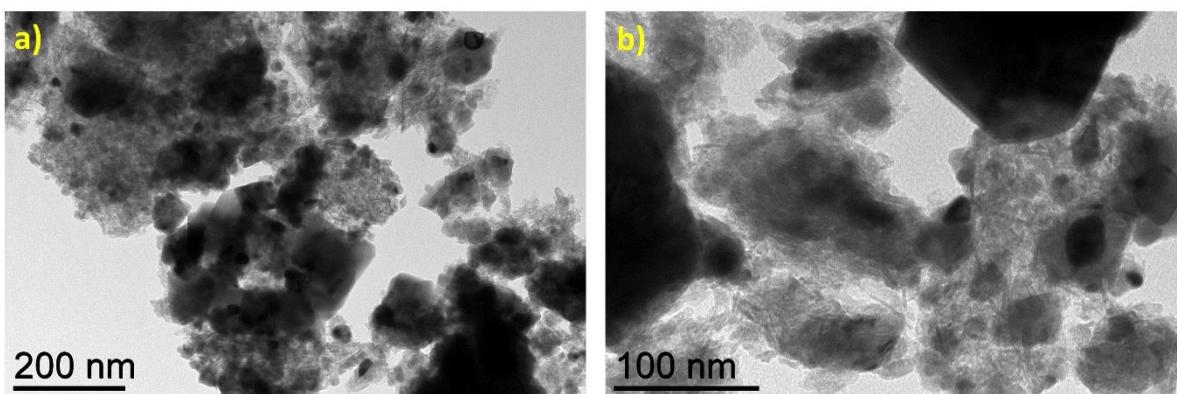**Figure S27.** Spent catalyst Fe$_{2.2}$C/Siralox, a,b) BFTEM image.

Figure S28. Spent catalyst Fe$_{2.2}$C@Mo-IH/Siralox, a,b) BFTEM image.

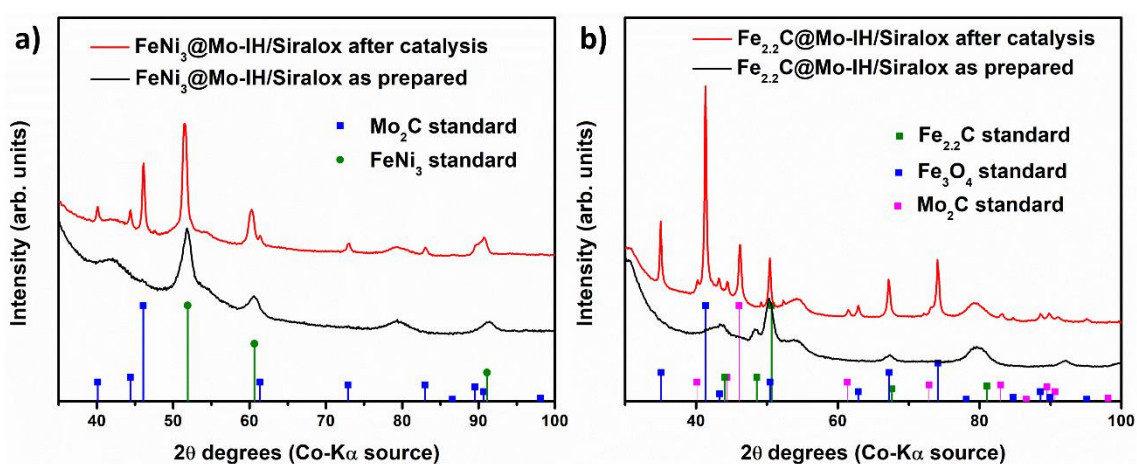**Figure S29.** Overlay of the powder XRD patterns of catalysts before (black trace) and after (red trace), a) FeNi$_3$@Mo-IH/Siralox (ICDD: 00-038-0419, standard pattern of FeNi$_3$ shown as green vertical drop lines; ICDD: 00-035-0787, standard pattern of Mo$_2$C shown as blue vertical drop lines), and b) Fe$_{2.2}$C@Mo-IH/Siralox (ICDD: 00-036-1249, standard pattern of Fe$_{2.2}$C shown as green vertical drop lines; ICDD: 00-035-0787, standard pattern of Mo$_2$C shown as magenta vertical drop lines; ICDD: 00-019-0629, standard pattern of Fe$_3$O$_4$ shown as blue vertical drop lines).

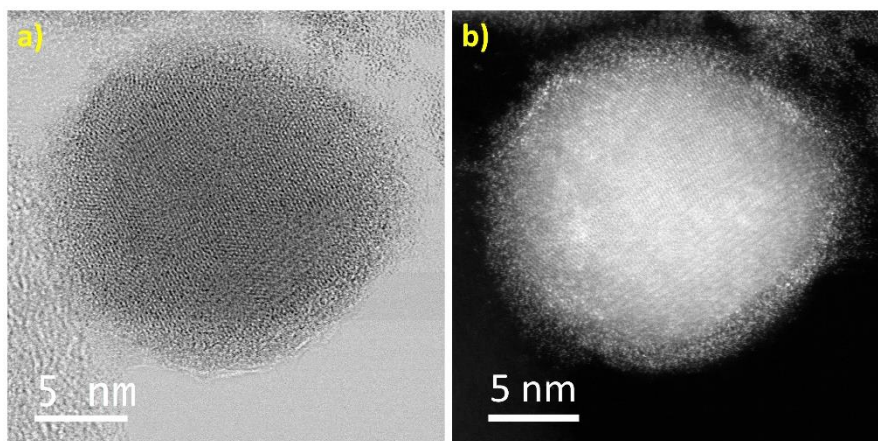## 2.12. Characterization of FeNi$_3$@WO$_x$-IH NPs

Figure S30. FeNi$_3$@WO$_x$-IH NPs, a) HR-STEM image, and b) HR-STEM HAADF image. The presence of the W at the outer surface was quite evident (bright spots).
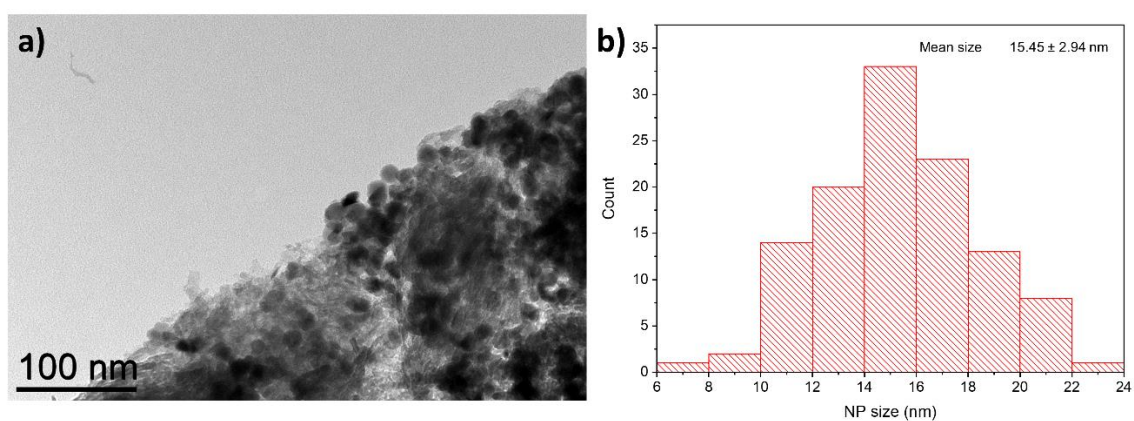

Figure S31. As prepared FeNi$_3$@WO$_x$-IH/Siralox, a) BFTEM image, and b) particle size distribution.
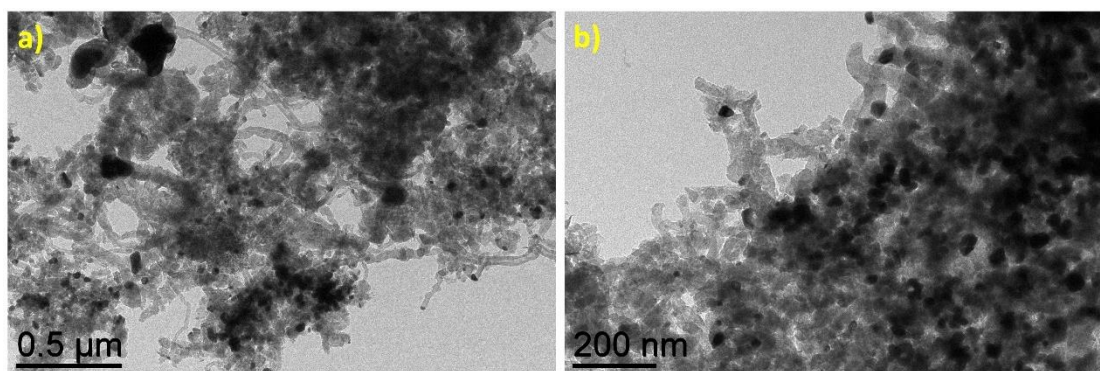

Figure S32. Spent catalyst FeNi$_3$@WO$_x$-IH/Siralox, a,b) BFTEM image.

References

1. D. De Masi, J. M. Asensio, P. -F. Fazzini, L. -M. Lacroix and B. Chaudret, *Angew. Chem. Int. Ed.,* 2020, **59**, 6187–6191.

2. A. Bordet, L. -M. Lacroix, P.-F. Fazzini, Dr. J. Carrey, K. Soulantica and B. Chaudret, *Angew. Chem. Int. Ed.,* 2016, **55**, 15894–15898.

3. Y. S. Mok, E. Jwa, and Y. J. Hyun, *J. Energy Chem.*, 2013, **22**, 394-402.

4. J. Baltrusaitis, B. Mendoza-Sanchez, V. Fernandez, R. Veenstra, N. Dukstiene, A. Roberts and N. Fairley, *Appl. Surf. Sci.*, 2015, **326**, 151–161.

5. M. Watschinger, K. Ploner, D. Winkler, J. Kunze-Liebhäuser, B. Klötzer and S. Penner, *Rev. of Sci. Instruments,* 2021, **92**, 2, 024105.

6. J.-H. Huang, H.-H. Hsu, D. Wang, W.-T. Lin, C.-C. Cheng, Y.-J. Lee and T.-H. Hou, *Sci. Rep.,* 2019, **9**, 1-8.

7. Z. Wang, F. Di-Franco, A. Seyeux, S. Zanna, V. Maurice and P. Marcus, *J. Electrochem. Soc.,* 2019, **166**, C3376.

8. F. G. Baddour, E. J. Roberts, A. T. To, L. Wang, S. E. Habas, D. A. Ruddy, N. M. Bedford, J. Wright, C. P. Nash, J. A. Schaidle, R. L. Brutchey and N. Malmstadt, *J. Am. Chem. Soc.*, 2020, **142**, 1010-1019.

9. J. Chen, C. Chen, Y. Chen, H. Wang, S. Mao and Y. Wang, *J. Catal.,* 2020, **392**, 313–321.

10. A. V. Okotrub, O. V. Sedelnikova, D. V. Gorodetskiy, A. D. Fedorenko, I. P. Asanov, Y. N. Palyanov, A. V. Lapega, O. A. Gurova and L. G. Bulusheva, *Materials*, 2023, **16**, 1650.

11. K. Murugappan, E. M. Anderson, D. Teschner, T. E. Jones, K. Skorupska and Y. Román-Leshkov, *Nat. Catal.,* 2018, **1**, 960-967.

12. P. Delporte, C. Pham-Huu, P. Vennegues, M. J. Ledoux and J. Guille, *Catal. Today*, 1995, **23**, 251-267.

13. E. D. Ochoa, D. Torres, R. Moreira, J. L. Pinilla and I. Suelves, *Appl. Catal. B: Environ.,* 2018, **239**, 463-474.